The Flexiscope: a Low Cost, Flexible, Convertible, and Modular Microscope with Automated Scanning and Micromanipulation.

Amy Courtney[1]*, Luke M. Alvey[1], George O.T. Merces[1], and Mark Pickering[1].

[1]School of Medicine, University College Dublin, Ireland.

*Correspondence: amy.courtney@ucdconnect.ie

Abstract

With technologies rapidly evolving, many research institutions are now opting to invest in costly, high-quality, specialised microscopes which are shared by many researchers. As a consequence, the user does not have the ability to adapt a microscope to their specific needs and limitations in experimental design are introduced. A flexible work-horse microscopy system is a valuable tool in any laboratory to meet the diverse needs of a research team and promote innovation in experimental design. We have developed the Flexiscope; a multi-functional, adaptable, efficient and high performance microscopy/electrophysiology system for everyday applications in a neurobiology laboratory. The core optical components are relatively constant in the three configurations described here; an upright configuration, an inverted configuration and an upright/electrophysiology configuration. We have provided a comprehensive description of the Flexiscope. We show that this method is capable of oblique infrared illumination imaging, multi-channel fluorescent imaging, and automated 3D scanning of larger specimens. Image quality is conserved across the three configurations of the microscope, and conversion between configurations is possible quickly and easily, while the motion control system can be repurposed to allow sub-micron computer-controlled micromanipulation. The Flexiscope provides similar performance and usability to commercially available systems. However, as it can be easily reconfigured for multiple roles, it can remove the need to purchase multiple microscopes, giving significant cost savings. The modular re-configurable nature allows the user to customise the system to their specific needs and adapt/upgrade the system as challenges arise.

1. Introduction

Microscopy is widely regarded as a centrally important technique in all areas of biological research. The ability to resolve structures which would have otherwise been invisible to our eyes has contributed to the advancement of many fields. Specifically, the fundamental components of the brain, neurons, were identified by Golgi and Cajal using this technique. Neuroscience today has been propelled by the advancement of microscopes to perform functional measurements and connectomic studies (Jorgenson et al., 2015).

With technologies rapidly evolving, many research institutions are now opting to invest in high-cost, high-quality, specialised microscopes which are shared by many researchers. As a consequence, an individual user does not have the ability to adapt a microscope to their specific needs and limitations in experimental design are introduced from the outset. Each experimental design has an optimal opto-mechanical configuration, and the possible variations are diverse. For example, electrophysiology experiments frequently require a fixed specimen stage and motion control of the microscope. In contrast, fluorescent or differential interference contrast (DIC) microscopy usually requires motion control of the specimen stage and a fixed microscope. Depending on the sample, an upright or inverted objective orientation may be optimal. Many experiments also involve coupling a microscope with other equipment such as a micromanipulator or incubator. Multiple microscopes would be required for each application despite the fact that many elements would be duplicated across the configurations. An adaptable work-horse microscopy system is a crucial and invaluable tool in any laboratory to meet the diverse needs of a research team and promote innovation in experimental design.

With flexibility and funding limitations in mind, many researchers have devised excellent cost-saving strategies which include 3D printed microscopes and XYZ translators (Sharkey et al., 2016),(Baden et al., 2015) (Maia Chagas et al., 2017), (Stewart and Giannini, 2016), a $0.58 origami microscope (Cybulski et al., 2014), and modifications to old microscopes (Peidle et al., 2009), (Hernández Vera et al., 2016), (Stewart and Giannini, 2016). These types of systems are advantageous in the field or within incubators but their low cost often equates to a compromise in image quality

and a lack of long term stability. In addition, many labs do not have access to these salvaged components or 3D printers and therefore reproducibility can be challenging. The components used to construct a flexible microscopy system must be readily available to research groups around the world, the system must cost considerably less than a commercial system while also maintaining a comparable image quality.

We have designed, constructed and extensively tested a high quality, transformable microscopy system assembled from optical and mechanical components. The core optical components remain constant while alterations are made for specialised experimental set-ups, including objective orientation and which components are fixed or translating. The use of commercially available opto-mechanical elements offers many advantages including ease of use, reliable alignment and reproducibility (both within and between laboratories) due to the availability and compatibility of the parts. The modular, re-configurable nature allows the user to customise the system to their specific needs and adapt the system to the everyday diverse challenges faced when attempting to answer complex neurobiological questions. This system can also be expanded to cope with new experimental challenges and upgraded as technologies rapidly evolve, a considerable advantage over static commercial systems. The flexibility of our modular microscopy system allowed us to also implement automated stage scanning and image acquisition. A commercial microscope would often require expensive and manufacturer-specific control software. Further cost savings are achieved as many components can be designated for multiple applications, such as the actuators used to control the automated specimen stage which can be easily re-configured as a micromanipulator.

We have provided a comprehensive description of a multi-functional, custom-built, adaptable, efficient and high-performance microscopy/electrophysiology system for both standard and unconventional applications in a neurobiology laboratory. This system encompasses the capabilities of multiple microscopes with considerable cost and space savings. Our system can be directly replicated or adapted to suit the needs any research group. Key characteristics of **'The Flexiscope'** include: ease of use; upright and inverted configurations allowing multi-angle imaging; fluorescent microscopy; automated stage scanning; visualisation of unstained tissue; sub-micron

computer-controlled micromanipulation. Implementation of this system does not require any specialised skills or knowledge.

2. Materials and methods

2.1 Parts and Components

In order to thoroughly detail every component of the Flexiscope, each individual part has been allocated a part designation, for use throughout this description. Table 1 lists each part and its designation, in addition to the suppliers, supplier part number, and cost of each part.

Table 1. Flexiscope Component List with Designators and a Cost Description.

Component	Part Designator	Component Description	Product Code	Supplier	Quantity	Cost per unit (€)	Total cost (€)
Core Optical Components							
Fluorescence Illumination Module	CO1	Lime (565 nm) Mounted LED	M565L3	Thorlabs	1	186.10	186.10
	CO2	Blue (470 nm) Mounted LED	M470L3	Thorlabs	1	236.38	236.38
	CO3	UV (395 nm) Mounted LED	M395L4	Thorlabs	1	249.61	249.61
	CO4	LED Driver	LEDD1B	Thorlabs	3	258.43	775.29
	CO5	Power Supply for LED and Piezo T-Cubes	TPS008	Thorlabs	1	158.76	158.76
	CO6	Aspheric Condenser Lens (for LED collimation)	ACL2520U-DG6-A	Thorlabs	3	24.43	73.29
	CO7	Dichroic mounting cube	CM1-DCH/M	Thorlabs	2	139.36	278.72
	CO8	GFP Dichroic Filter (Refl. Band = 452-490 nm, Trans. Band = 505-800 nm)	MD498	Thorlabs	1	188.87	188.87
	CO9	BFP Dichroic Filter (Refl. Band = 360-407 nm, Trans. Band = 425-575 nm)	MD416	Thorlabs	1	188.87	188.87
	CO10	Iris Diaphragm	SM1D12D	Thorlabs	1	56.71	56.71
Infinite Space Module	CO11	Protected Silver Tuning Mirror	CCM1-P01/M	Thorlabs	1	144.90	144.90
	CO12	Texas Red Filter Set (Excitation, Emission, and Dichroic)	MDF-TXRED	Thorlabs	1	551.25	551.25
	CO13	FITC Filter Set (Excitation, Emission, and Dichroic)	MDF-FITC	Thorlabs	1	551.25	551.25
	CO14	BFP Texas Red Filter Set (Excitation, Emission, and Dichroic)	MDF-BFP	Thorlabs	1	551.25	551.25
	CO15	Swappable Filter Set Mount	DFMT1	Thorlabs	3	177.28	531.84
	CO16	Filter Mount Holding Cube	DFMB/M	Thorlabs	1	90.85	90.85
	CO17	Filter Cube Blank Top Plate	DFM1C	Thorlabs	1	32.40	32.40
	CO18	Objective Lens Turret	OT1	Thorlabs	1	262.53	262.53
	CO19	4X Olympus Plan Achromat Objective (NA=0.10, WD=18.5 mm)	RMS4X	Thorlabs	1	167.07	167.07
	CO20	20X Olympus Water Immersion Objective (NA=0.5, WD=3.5 mm)	UMPLFLN20XW	Masons	1	1,176.68	1,176.68
Camera Module	CO21	Tube lens: Achromatic Doublet (f=150.0 mm)	AC254-150-A	Thorlabs	1	62.56	62.56
	CO22	USB 3.0 Monochrome Camera (Flea®3 ⅟" FL3-U3-13Y3M-C)	86-767	Edmund Optics	1	783.75	783.75
	CO23	USB 3.0 Color Camera (Grasshopper GS3-U3-1555C-C 2/3")	33-533	Edmund Optics	1	1,435.09	1,435.09
	CO24	1" Lens Tube to C-Mount Adapter (Male to Male)	SM1A39	ThorLabs	1	18.60	18.60
	CO25	USB 3.0 Locking Cable	86-770	Edmund Optics	1	23.75	23.75
	CO26	Infrared LED array	N/A	Salvaged from CCTV Camera	1	N/A	N/A
Coupling and Alignment	CO27	Male to Male Tube Coupler (0.5")	SM1T2	Thorlabs	6	17.55	105.30
	CO28	Male to Male Tube Coupler (2")	SM1T20	Thorlabs	1	18.74	18.74
	CO29	Cage Cube Connector	C4W-CC	Thorlabs	1	43.57	43.57
	CO30	Alignment Posts (Diameter = 6 mm, L = 75 mm)	MS3R/M	Thorlabs	4	7.10	28.40
	CO31	1" Threaded Cage Plate (0.50" Thick)	CP02T/M	Thorlabs	1	17.90	17.90
	CO32	1" Threaded Cage Plate (0.35" Thick)	CP02/M	Thorlabs	2	14.11	28.22
	CO33	1" Lens Tube, 0.30" Thread Depth	SM1L03	Thorlabs	4	10.72	42.88
	CO34	1" Lens Tube, 0.5" Thread Depth	SM1L05	Thorlabs	3	11.33	33.99
	CO35	1" Lens Tube, 3" Thread Depth	SM1L30	Thorlabs	1	21.95	21.95
	CO36	1" Lens Tube, 0.31" Travel Range (Adjustable)	SM1V05	Thorlabs	2	26.11	52.22
	CO37	1" Lens Tube, 0.81" Travel Range (Adjustable)	SM1V10	Thorlabs	1	29.34	29.34
	CO38	Plastic Dust Cap for 1" Lens Tubes	SM1EC2	Thorlabs	10	1.76	17.64
	CO39	1" Lens Tube, 1.5" Thread Depth	SM1L15	Thorlabs	1	14.27	14.27
Other components							
Motion Control Components	MC1	Lab Jack	L490/M	Thorlabs	1	527.40	527.40
	MC2	Piezoelectric Actuator (13 mm Travel)	PIA13	Thorlabs	4	440.12	1,760.48
	MC3	T-Cube: Piezoelectric Actuator Controller	TIM101	Thorlabs	1	837.90	837.90
	MC4	13 mm XYZ Translation Stage	MT3/M	Thorlabs	1	798.21	798.21
	MC5	13 mm Translation Stage Plate in One Dimension	MT1A/M	Thorlabs	1	356.00	356.00
	MC6	25 mm XYZ Translation Stage	PT3A/M	Thorlabs	1	954.00	954.00
Mounting Components	MO1	Optical Post (Ø12.7 mm, L = 30 mm)	TR30/M-P5	Thorlabs	5	3.84	19.20
	MO2	Optical Post (Ø12.7 mm, L = 20 mm)	TR20/M-P5	Thorlabs	5	3.76	18.82
	MO3	Optical Post (Ø12.7 mm, L = 50 mm)	TR50/M-P5	Thorlabs	5	4.12	20.60
	MO4	Optical Post (Ø12.7 mm, L = 75 mm)	TR75/M-P5	Thorlabs	5	4.39	21.95
	MO5	Optical Post (Ø12.7 mm, L = 100 mm)	TR100/M-P5	Thorlabs	5	4.50	22.52
	MO6	Optical Construction Post for TR75C/M (Ø12.7 mm)	TR75T/M	Thorlabs	1	14.90	14.90
	MO7	Optical Construction Post- Variable Angle (Ø12.7 mm)	TR75C/M	Thorlabs	1	14.90	14.90
	MO8	Post Holders (Ø12.7 mm, L=30 mm)	PH30/M-P5	Thorlabs	5	6.33	31.64
	MO9	Post Holders (Ø12.7 mm, L=20 mm)	PH20/M-P5	Thorlabs	5	6.20	31.01
	MO10	Post Holders (Ø12.7 mm, L=50 mm)	PH50/M-P5	Thorlabs	5	6.79	33.96
	MO11	Post Holder (Ø12.7 mm, L=75 mm)	PH75/M-P5	Thorlabs	5	7.05	35.25
	MO12	Mounting Base (25 mm x 75 mm x 10 mm)	BA1/M-P5	Thorlabs	5	4.45	22.23
	MO13	Mounting Base (25 mm x 58 mm x 10 mm)	BA1S/M-P5	Thorlabs	5	3.99	19.94
	MO14	Mounting Base (50 mm x 75 mm x 10 mm)	BA2/M-P5	Thorlabs	5	5.80	28.98
	MO15	Breadbord (100 mm x 150 mm x 12.7 mm)	MB1015/M	Thorlabs	1	36.90	36.90
	MO16	Base Plate for Z-Axis Stage Mounting (65 mm x 65 mm x 10 mm)	UBP2/M	Thorlabs	1	30.87	30.87
	MO17	Right-Angle Bracket	AB90C/M	Thorlabs	2	22.67	45.34
	MO18	Microscopy Slide Holder	MAX3SLH	Thorlabs	1	105.69	105.69
	MO19	Composite Core Optical Breadboard (600 x 600 x 28 mm)	M-TD-22	Newport	1	488.70	488.70
	MO20	Sorbothane Feet (Ø27.0 mm)	AV4/M	Thorlabs	4	4.69	18.74
Blackout Enclosure	BE1	Black Hardboard (610 mm x 610 mm, 5 mm Thick)	TB4	Thorlabs	3	18.81	56.43
	BE2	Aluminium Extrusion (25 x 25mm, L = 600 mm)	XE25L600/M	Thorlabs	8	25.52	204.16
	BE3	Vertical Blackout Blind (600 mm x 1700 mm)	VB8060	Thorlabs	2	88.11	176.22
	BE4	Black Masking Tape (50mm x 55m)	T137-2.0	Thorlabs	1	13.86	13.86
Head Stage Mounting	HS1	Male M6 to Female M4 Coupler	AS4M6M	Thorlabs	2	3.81	7.62
	HS2	Male M4 to Female M3 Coupler	MS4A/M	Thorlabs	2	4.17	8.34
	HS3	45° Brackets	100281	MakerBeam	12	0.58	6.95
	HS4	Aluminum Extrusion (10x10mm, L= 100mm)	100078	MakerBeam	16	0.58	12.25
Additional configuration parts							
3D printed Components	3D1	Swappable Filter Set Mount Holder	*For 3D model files, see supplementary file 3*		3	N/A	N/A
	3D2	Lens Tube - Part1			1	N/A	N/A
	3D3	Lens Tube - Part2			1	N/A	N/A
	3D4	Camera Alignment			1	N/A	N/A
	3D5	Coupler: Actuator to Stepper			3	N/A	N/A
	3D6	Y-axis Mounting			1	N/A	N/A
	3D7	Z-axis Mounting			1	N/A	N/A
Stepper Motor XYZ-Stage	S1	Arduino Uno	A000066	Farnell	1	17.15	17.15
	S2	CNC Shield V3.0	N/A	gearbest.com	1	4.28	4.28
	S3	DRV8825 Motor Drivers	RB-Pol-272	RobotShop	5	1.44	7.19
	S4	Jumpers	791-6454	Radionics	20	0.23	4.62
	S5	NEMA17 Stepper Motor 1.8°, 0.22nm, 2.8 V, 1.33 A, 4 Wire	535-0467	Radionics	3	24.09	72.27
	S6	Male USB A to Male USB B	529-8274	Radionics	1	6.21	6.21
	S7	Female Shorting Link	251-8682	Radionics	10	0.03	0.27
	S8	12V Power Supply	148-963	Radionics	1	12.89	12.89
	S9	Spiral Binding	446-172	Radionics	1	7.21	7.21
	S10	Bearings	100438	MakerBeam	10	1.40	14.00
	S11	NEMA17 Stepper Bracket	100225	MakerBeam	3	3.50	10.50
	S12	90° Brackets	100304	MakerBeam	12	0.58	6.95
	S13	Right Angle Brackets	100326	MakerBeam	12	0.58	6.95
	S14	100mm Anodised MakerBeam	100078	MakerBeam	16	0.77	12.25
	S15	60mm Anodised MakerBeam	100056	MakerBeam	8	0.38	3.00
	S16	40mm Anodised MakerBeam	100056	MakerBeam	8	0.38	3.00

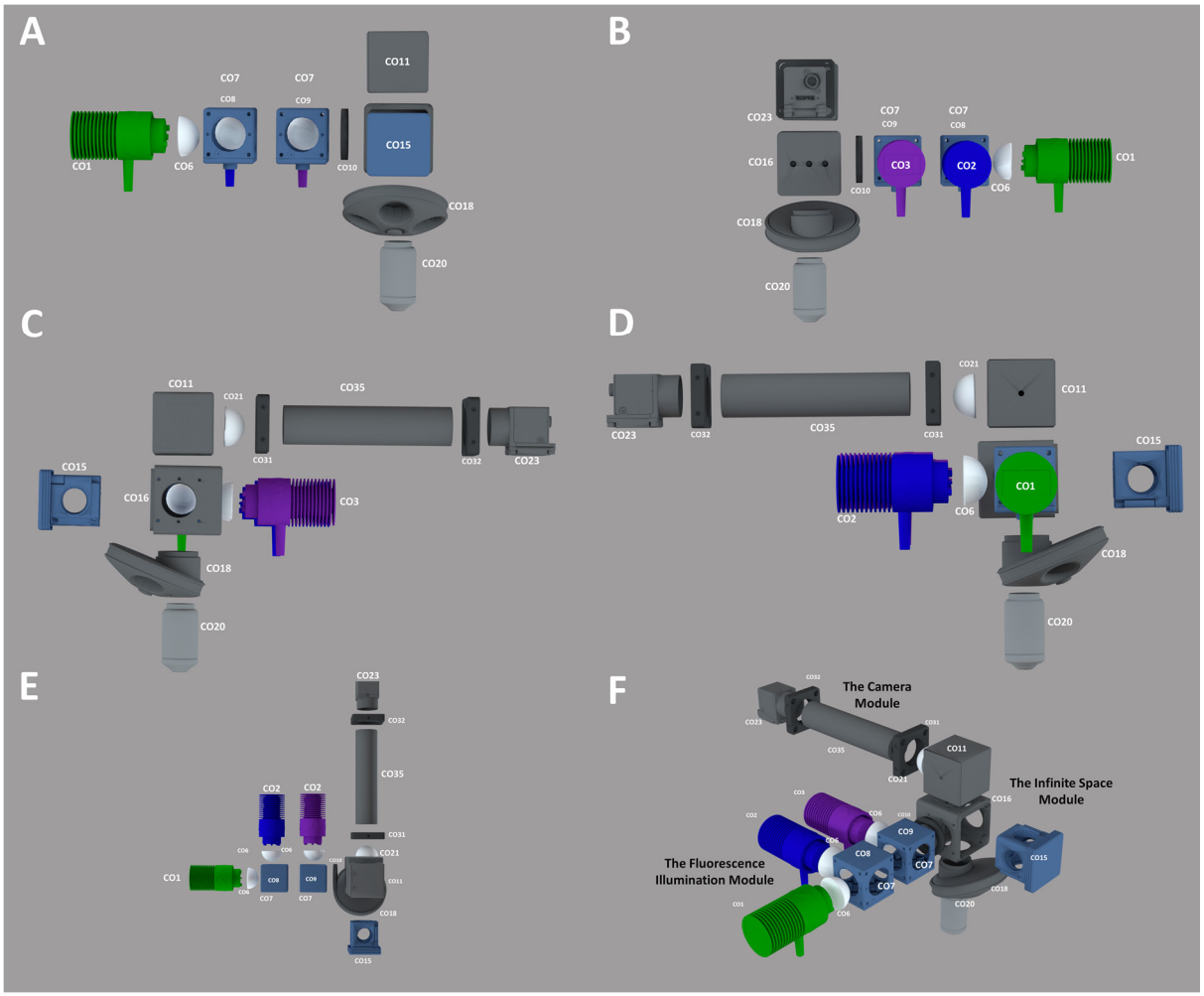

Figure 1. Core Optical Components of the Flexiscope. The key optical and mechanical components constituting the light path of the Flexiscope illustrated schematically. The core optical components remain relatively constant with each configuration. Depending on the application, alterations are made to the mounting and motion control of specific elements. (A-D) illustrates the four side-views of the core optical components of the Flexiscope. (E) Illustrates a top-view of the core optical components of the Flexiscope. (F) Illustrates an orthogonal-view of the core optical components of the Flexiscope. The system can be divided into three functional modules; the fluorescence illumination module, the infinite space module, and the camera module. Component labels correspond to Table 1.

The Core Optical Components

We describe three sample configurations of the Flexiscope, differing in objective orientation, mounting and motion control. Within each configuration the core optical components remain relatively constant (Figure 1). The core optical components can be divided into three functional units: the fluorescence illumination module, the infinite space module and the camera module.

The Fluorescence Illumination Module

Fluorescent excitation is provided by three independent high intensity LEDs collimated with aspheric condenser lenses (CO6). They are combined into a single beam (Figure 1, E and F) using two dichroic mirrors (CO8 and CO9) positioned at 45º to the light path in a mounting cube (CO7). The dichroic mirrors have 452-490nm reflection/505-800nm transmission and 360-407nm reflection/425-575nm transmission bands respectively. This results in the 565nm LED (CO1) passing through both dichroics, the 470nm (CO2) reflecting off the first dichroic and passing through the second dichroic while the 395nm (CO3) LED reflects off the second dichroic. An iris (CO10) is placed after the LED module before the filter mount-holding cube (CO16) to allow for regulation of excitation light. The excitation light is then directed towards the filter mount-holding cube (CO16). The filter mount-holding cube holds the swappable filter set mounts (CO15), which are pre-configured to contain an excitation, emission and dichroic filter corresponding to either 630nm (Texas Red, CO12), 530nm (FITC, CO13) or 460nm (BFP, CO14) emission wavelengths. When the light passes through the excitation filter the dichroic mirror inside the filter set mount directs the light towards the objective lens. The fluorescence illumination module is a fixed entity, regardless of the desired application.

The Infinite Space Module

The Flexiscope is designed to use infinite conjugate objectives. The space between the tube lens and the objective (the infinite space module, Figure 1 F) can be modified to the user's needs with minimal impact on optical performance. Two Infinite conjugate objectives, a 4X Olympus plan achromat objective (numerical aperture (NA) = 0.10, CO19) and a 20X Olympus water immersion objective (NA = 0.5, CO20), are coupled to a lens turret (CO18). The light path then travels vertically from the specimen, through the objective, through the filter set mount emission filter to the 45° turning mirror (CO11). The mirror directs the light path horizontally towards the achromatic doublet (CO21), which acts as a tube lens.

The Camera Module

The elements found immediately after the achromatic doublet lens comprise the camera module (Figure 1, E and F). The distance between the achromatic doublet lens and the camera sensor is fixed at 150mm using adjustable length lens tubes

(CO28, CO35 and CO37). Transmitted or reflected light imaging can be achieved by leaving the filter mount holding cube empty and enclosing the opening with the filter cube blank top plate (CO17). Oblique infrared illumination microscopy (OIR) uses infrared LEDs (CO26) at an angle above or below the specimen which allows the visualisation of 3D structures, resulting in images similar in appearance to DIC microscopy (Alix et al., 2003) (Beltran-Parrazal et al., 2014). All cameras used are c-mount machine vision cameras from Point Grey (now owned by FLIR). A high frame rate, mono, infrared sensitive camera is used for OIR (CO22). A high sensitivity, low noise, colour camera is used for fluorescence detection (CO23). The entire system is coupled together using 1" diameter lens tubes, with c-mount adaptors (CO24) used to couple the c-mount cameras.

2.2 Motorised Motion Control and Automated Image Acquisition

Our motion control system was designed to allow precise, repeatable and controllable movement of the specimen stage. The system can be controlled using customisable Matlab scripts and linked to image acquisition to permit fully automated scanning of larger samples.

The Piezoelectric Stage

Piezoelectric actuators (MC2) control the three dimensions of motion of the specimen stage while the Flexiscope is in the upright or inverted configuration. This allows X-motion (stage: right/left), Y-motion (stage: forward/backward) and Z-motion (stage: up/down) control. A controller module (MC3) allows computer control of the actuators. The APT software (ThorLabs) allows control of the actuators through the controller module. The ActiveX control capability in Matlab allows control of the actuators via the APT software. The image acquisition toolbox in Matlab is also capable of controlling the PointGrey cameras used on our microscope, so automated scanning is operated within Matlab's workspace.

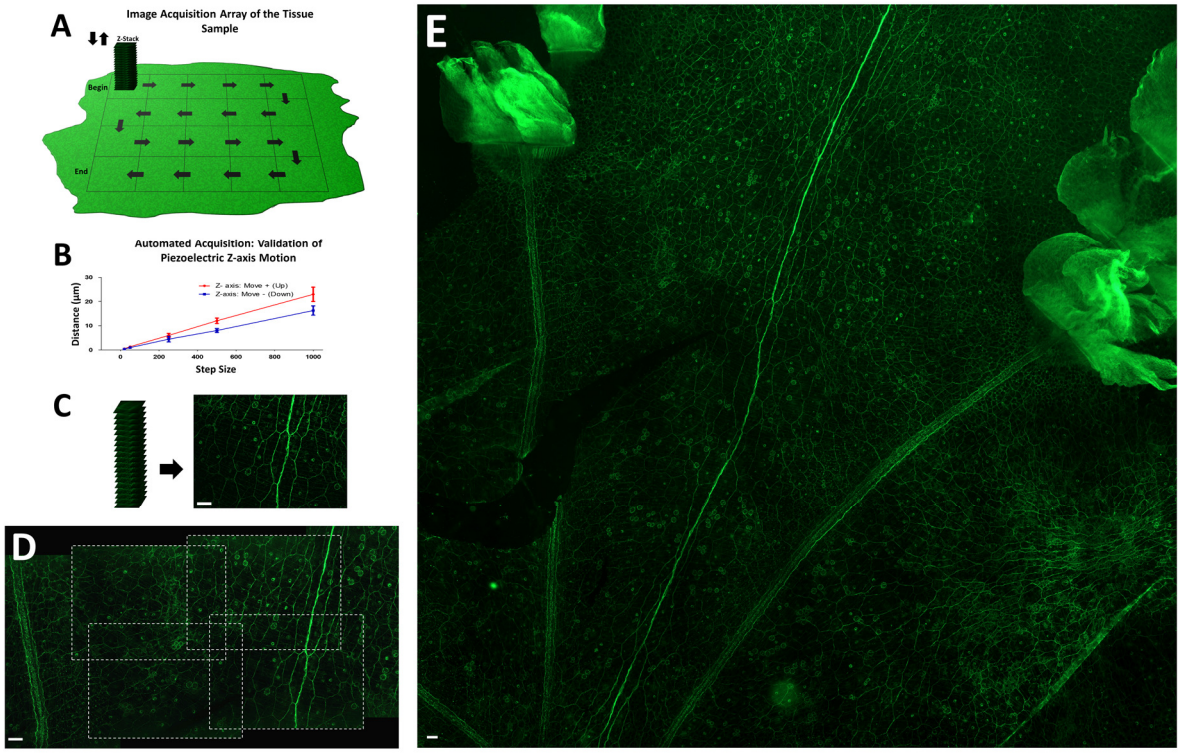

Figure 2. Validation of Automated Specimen Stage Motion Control and Image Acquisition. (A) Schematic representation of the automated stage motion control workflow to acquire Z-stacks at regions of the sample in the X and Y direction. Many factors can influence piezoelectric actuator function and as the 'step size' values are arbitrary we acquired video recordings of the stage during motion and manually calculated the distance in ImageJ (Rueden et al., 2017). The following parameters were also set through the APT software; voltage (V): 110, drive rate (steps/sec): 500, drive accn (steps/sec/sec): 100000 and jog rate (steps/sec):500. Load can alter piezoelectric actuator function and thus the load of the Z-axis is ~ 335g. (B) Validation of mean distance (µm) travelled by the Z-axis piezoelectric actuator when specific 'step size' commands (20, 50, 250, 500 and 1000) are executed repeatedly (n=15). The error bars indicate standard deviation and thus the intrinsic lack of repeatability of these actuators is evident. The resolution limit did not enable individual step distance discrimination for the 20 and 50 'step sizes' and therefore standard deviation could not be acquired. The distance travelled when the stage is moving up is greater than the distance travelled when the stage is moving down, despite the same command being sent to the actuators. (C) Example of 20 images (Z-stack) acquired at each step in the Z-dimension to acquire multiple in-focus planes in the tissue sample. The corresponding maximum intensity projection is seen alongside the Z-stack. This allows the 3D tissue to be visualised as a 2D image (Forster et al., 2004). (D) Illustrates the overlap in each new FOV in the X and Y dimension and enables image stitching. Image E is a composites of 50 maximum intensity projection images stitched together in ImageJ ((Preibisch et al., 2009). Scale bar for all: 50µm.

The commands used to control the specimen stage followed a logic in which the image sequence of the tissue sample is considered a two dimensional array (Figure 2 A). To

acquire images of the whole tissue (or a region of interest) the stage is moved in the X-axis n-times in one direction, then moved in the Y-axis once and in the opposite direction in the X-axis n-times again. This cycle can then be repeated until the tissue has been imaged in its entirety. Each movement in X or Y dimension reveals a new 'field of view' (FOV) and a Z-stack is subsequently acquired (for code and detailed user guidelines see supplemental file 1).

The Stepper Motor Automated Scanning Stage

While the piezoelectric automated scanning stage was effective for our application (see 3.2) one major limitation became evident during extensive use; the piezoelectric actuators were slow. We therefore decided to re-configure the automated scanning stage to incorporate stepper motors (Supplementary Figure 2). This stage utilised 3D printed components to transform a manual XYZ translating stage with standard micrometers (MC4) into a motorised stage. Stepper motors are controlled using and arduino Uno running a gcode interpreter. Gcode is a standardised system for controlling XYZ position and movements commonly used in 3D printers and CNC machines. Control of the stage can then be achieved by issuing gcode commands. The system is controlled in Matlab in a manner similar to the piezoelectric configuration and the code/user guidelines are available in supplementary file 2.

2.3 Applications Of The Flexiscope: Transforming Between Configurations

A key design principle of a transformable microscope like the Flexiscope is that a single user should be able to convert from one mode of operation to another in a relatively short space of time, and without requiring specialised skills or tools. The core optical components are relatively constant in the following three modes of operation; the upright configuration, the inverted configuration and the upright/electrophysiology configuration, but differ primarily in mounting and motion control.

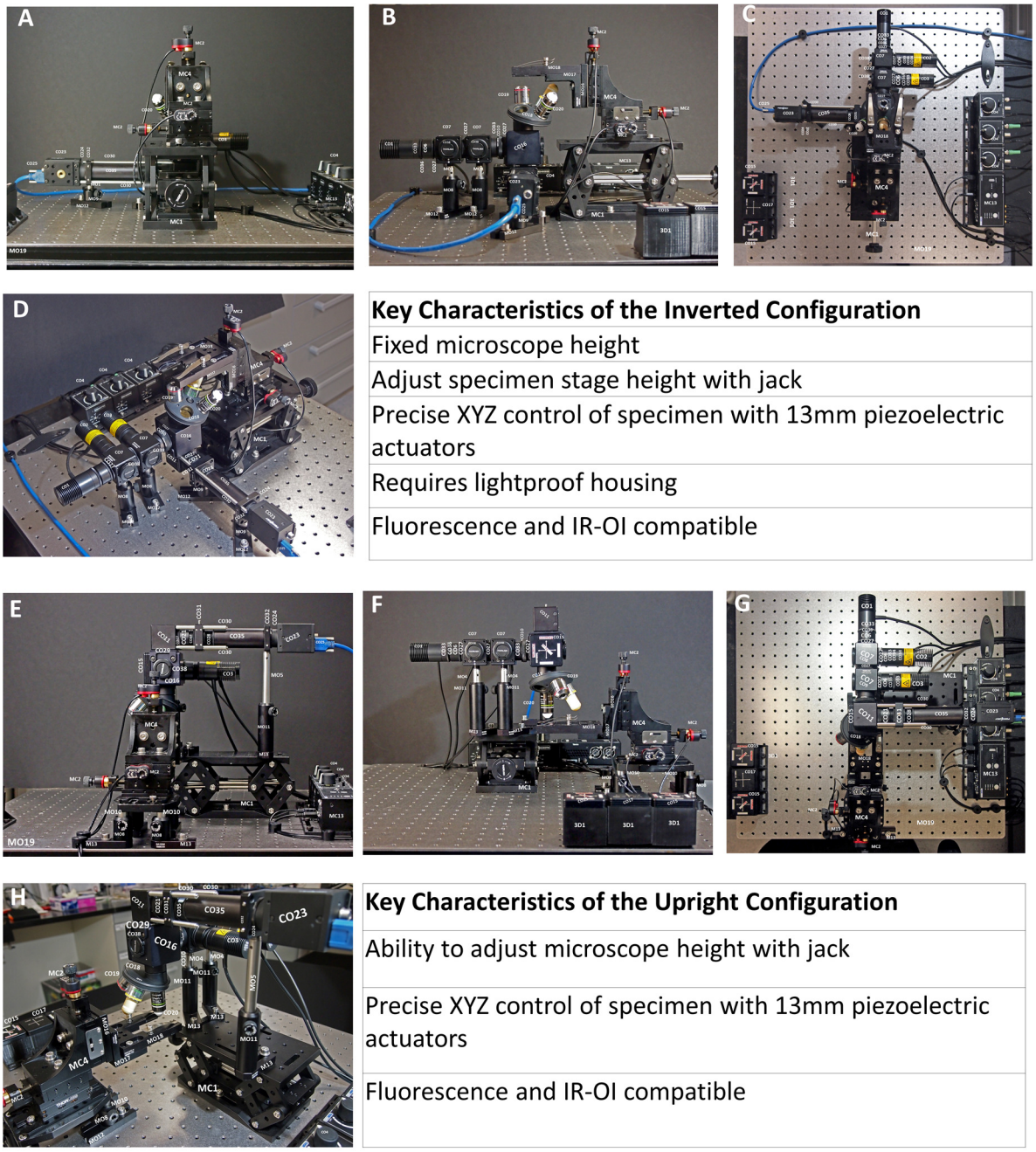

Key Characteristics of the Inverted Configuration
Fixed microscope height
Adjust specimen stage height with jack
Precise XYZ control of specimen with 13mm piezoelectric actuators
Requires lightproof housing
Fluorescence and IR-OI compatible

Key Characteristics of the Upright Configuration
Ability to adjust microscope height with jack
Precise XYZ control of specimen with 13mm piezoelectric actuators
Fluorescence and IR-OI compatible

Figure 3. Comparison of the Inverted and Upright Configurations of the Flexiscope. Photographs of the inverted (A-D) and upright (E-H) configurations illustrate the arrangement of the key optical and mechanical components of the flexiscope into commonly used set ups. Conversion between these configurations can be achieved in under 24 minutes (supplemental video 1). Key features of each configuration are listed alongside the photographs. Component labels correspond to Table 1.

Inverted to Upright Configuration in Under 30 Minutes

The steps required to transition from the inverted to upright configuration (Figure 3) involve firstly removing the XYZ specimen stage (MC4) from the jack (MC1). The jack

and the microscope can then be removed from the optical table (MO19). The microscope is simply rotated 180° so that the objectives are no longer facing vertically up, but now facing vertically down towards the optical table. Post and post holder height on the microscope is increased (MO11, MO5, MO4). The microscopy slide holder (MO18, MO17, MO16) on the specimen stage is reconfigured as seen in Figure 3 F. The specimen stage is mounted on a breadboard (MO15) with posts (MO10), post holders (MO8) and mounting bases (MO12, MO13). The microscope can then be mounted on the jack. Finally, the specimen stage and microscope/jack are aligned to one another before fixing all components to the optical table. This process takes under 24 minutes (Supplementary Video 1). Performing these steps in reverse will result in transformation from the upright to the inverted configuration.

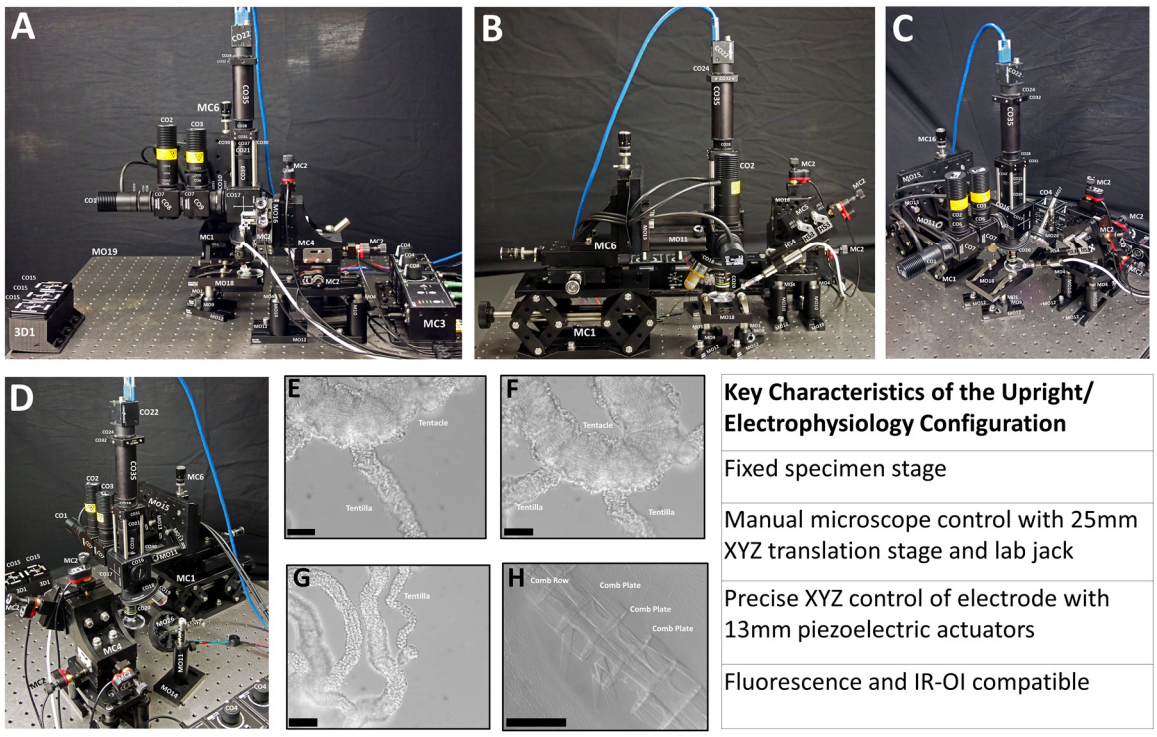

Figure 4. Configuring the Flexiscope for Electrophysiology Experiments and Demonstrating OIR Microscopy Capabilities of the System to Visualise Unstained Tissue. Photographs of the upright/electrophysiology configuration (A-D). Component labels correspond to Table 1. The key features of this configuration are listed alongside the photographs. The tentacles of *P. pileus* (gelatinous marine invertebrate) were used to demonstrate the capability of the Flexiscope in any configuration to implement OIR microscopy (E-G) Scale bar: 50µm. OIR microscopy to visualise the ciliary structures and body wall of *P. pileus* (H) scale bar: 500µm. OIR microscopy is performed by simply positioning Infrared LEDs obliquely above or below the tissue. No staining was required and the 3D architecture of the tissue could be appreciated.

The Upright/Electrophysiology Configuration: Manual Microscope Translation with a Four-Dimension Micromanipulator Controlled by Piezoelectric Actuators

The third configuration (upright/electrophysiology configuration, Figure 4.) requires some alterations to core optical components. For ease of mounting, in this configuration the light path is aligned vertically. To achieve this, the 45° mirror in the infinite space module is replaced with a 1.5" straight lens tube (CO39). In addition, the fluorescence illumination module is rotated so that the side mounted LEDs are oriented upwards. This modification is only required to facilitate mounting to the optical breadboard (MO15). The whole microscope is mounted to this breadboard which is in turn mounted vertically to a manual XYZ translation stage (MC6). The microscope components are mounted to the jack. A fixed specimen stage is mounted directly to the optical table.

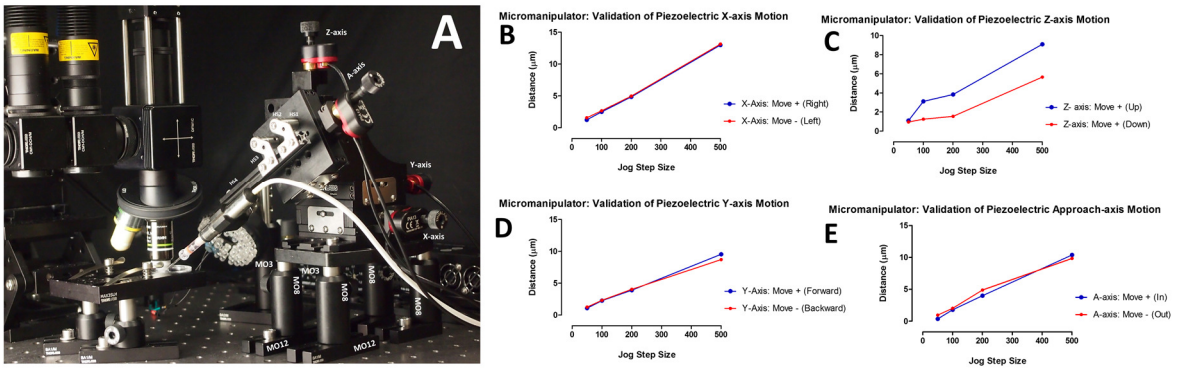

Figure 5. Micromanipulator Validation: Piezoelectric Actuation in Four Dimensions with <1µm resolution. Photograph of the XYZ stage and piezoelectric actuators configured as a micromanipulator. An additional axis known as the approach axis (A-axis) is incorporated to the stage to allow four dimension computerised motion control (A). Graphs B-E outlines the mean distance (µm) achieved when commands of a specific 'step size' were sent to the X, Y, Z and A-axis piezoelectric actuators respectively. Many factors can influence piezoelectric actuator function and as the 'step size' values are arbitrary we acquired video recordings of the stage during motion and manually calculated the distance in ImageJ (Rueden et al., 2017). The following parameters were also set through the APT software for each piezoelectric actuator; voltage (V): 110, drive rate (steps/sec): 500, drive accn (steps/sec/sec): 100000 and jog rate (steps/sec):100. Load can alter piezoelectric actuator function and thus the load of each axis was calculated; X-axis: ~1147g, Y-axis: ~692g, Z-axis:~435g and A-axis = ~85g.

Precise sub-micron micromanipulation of an electrode is imperative when undergoing electrophysiology experiments. However, such a tool can be extremely costly,

especially when computer controlled systems are required. The piezoelectric actuators which were previously configured as a specimen stage are now re-configured as a micromanipulator (Figure 5). A fourth dimension (approach-axis or A-axis, MC5) is incorporated into the stage and the angle of approach can be manually adjusted, depending on the objective configuration or to reduce the length of electrode in solution (minimise electrical noise). The electrode holder is mounted to the micromanipulator using Makerbeam and Thorlabs components (HS1-4). This configuration therefore involves a fixed specimen stage, manual microscope motion in three dimensions and four axis micromanipulation with <1µm step size (Supplementary Video 2).

2.4 Preparation of Tissue Samples for Validation

Pleurobrachia pileus Tissue Preparation

The ctenophore *Pleurobrachia pileus* (a gelatinous marine invertebrate) was collected from Howth Harbour, Dublin, Ireland [53°23'35.4"N 6°03'59.5"W 53.393158, -6.066533] between May and September 2017 using custom made plankton nets. Animals were maintained in a specialised aquarium system at 12-14°C in University College Dublin, Ireland for < 24 hours.

This animal possesses a decentralised neural network known as a 'nerve net' which is distributed across their spheroidal body, directly beneath the epithelial layer (Hernandez-Nicaise, 1973, Jager et al., 2011). Whole-mount immunofluorescence labelling of tyrosylated α-tubulin enables visualisation of their nervous system. Tissue was processed in a manner similar to (Jager et al., 2011). Animals were fixed using 50% natural seawater and 50% paraformaldehyde (PFA, 8%) in phosphate buffered saline (PBS) (Thermo Scientific, 10209252) at room temperature. Depending on animal size (blotted live weight: 0.047-1.249g) fixation occurred for 1-8 hours. Animals were dehydrated with 50% ethanol (100%) and 50% PBS for 15 minutes at room temperature then 100% methanol for 15 minutes at room temperature and stored in methanol at -20°C.

When the tissue was ready to be processed for immunofluorescence experiments rehydration to PBS was undertaken (the above dehydration steps in reverse). The tissue was dissected to enable 'flat' mounting of the outer epithelia layer to a glass slide. All internal anatomical structures (mesoglea, gastrovascular canals, tentacles,

tentacular sheaths, mouth and pharynx) were teased away with Dumont HP Tweezers (5 Carbon steel 0.08 x 0.04mm tip). The tissue was permeabilised with TritonX-100 (Sigma, Aldrich, T9284) at 0.2% and 0.1% in PBS for 30 minutes each on a rocking platform at room temperature. A fluorescent conjugated primary antibody against tyrosylated α-tubulin (Novus Biologicals, YL1/2, DyLight 488, NB600-506G) was diluted to 1:1000 in 1% BSA (Sigma-Aldrich, A7906) (diluted in 0.01% Triton-X100) and incubated in the fridge overnight. After washing the tissue in PBS three times for 10 minutes each, the tissue was placed epithelial layer up on a slide with OCT compound (VWR, 361603E) and sealed with a coverslip. This stabilises the tissue and allows 1-2 week storage in a humidity chamber in the fridge. Fluorescence imaging in all three configurations was tested with this tissue preparation at the same position to allow direct comparison.

Dorsal Root Ganglia Preparation

5 day old Wistar rat pups that were obtained from the Biomedical Facility in University College Dublin were euthanized in accordance with institute guidelines and relevant legislation (directive 2010/63/EU). Dorsal Root Ganglia (DRGs) dissected from the pups were cultured as explants for 6 days on flat laminin coated silicone substrates and fixed in PFA. Axons were labelled with 1:1000 Chicken anti neurofilament heavy (NFH) primary antibody (ab72996, Abcam), and 1:500 goat anti chicken IgY Alexa Fluor®568 secondary antibody (ab175477, Abcam). Cytoplasm of the cell bodies of migrating Schwann cells were labelled with 1:500 rabbit anti S100β primary antibody (ab52642, Abcam), and 1:500 Goat anti rabbit IgG Alexa Fluor®488 secondary antibody (A11008, Fisher Scientific). Nuclei of Schwann cells were labelled with the DNA label 10µg/ml DAPI (D9542, Sigma).

3. Results

3.1 Validation of Fluorescent and OIR Microscopy

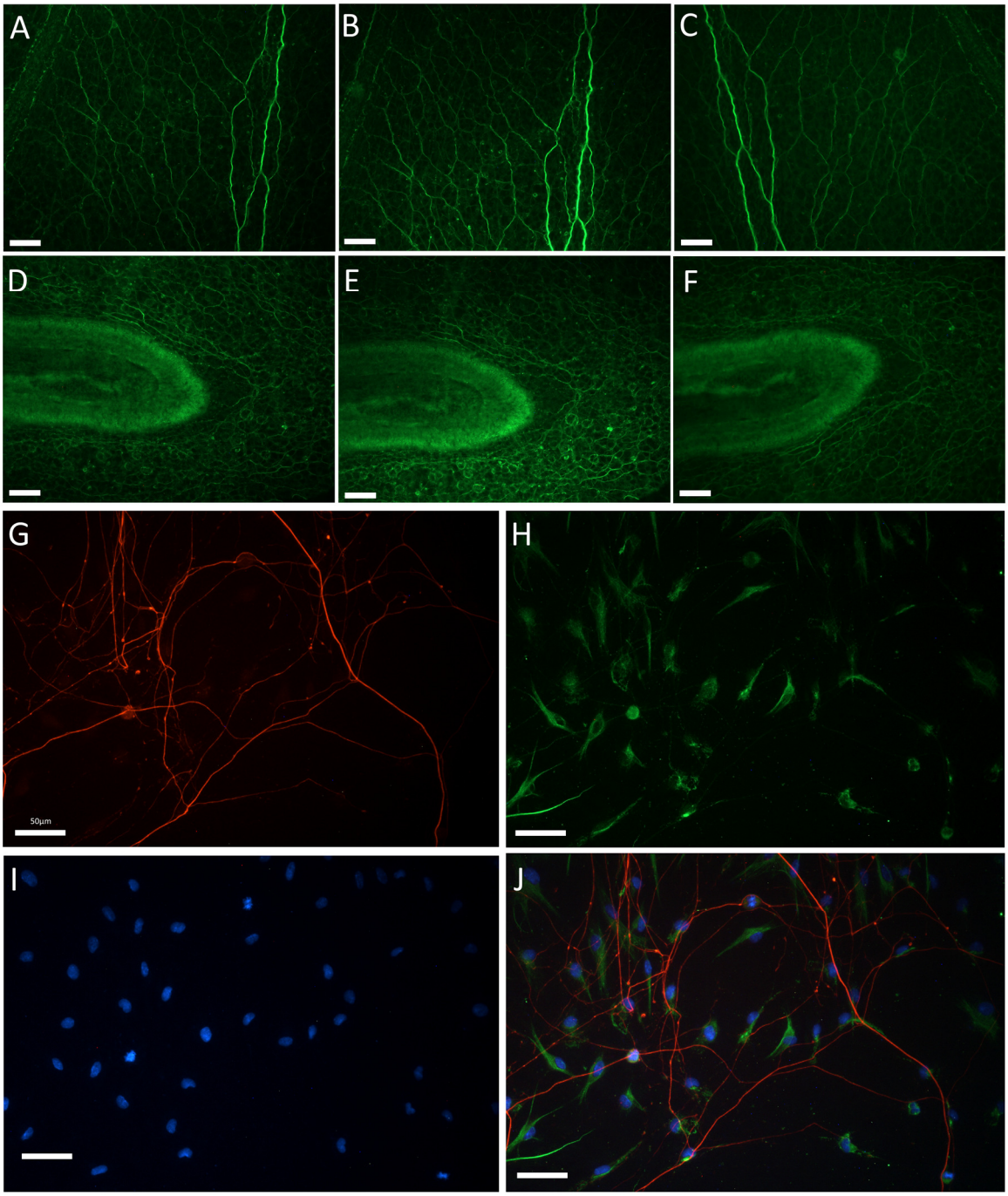

Figure 6. Comparison of Fluorescent Microscopy Performance in all Three Major Configurations and Demonstration of Three Channel Fluorescent Capabilities of the Flexiscope. Fixed whole mount *P. pileus* (gelatinous marine invertebrate) were labelled with an antibody against anti-tyrosylated α-tubulin. Image A and D were taken with the inverted Flexiscope configuration. Image B and E were taken with the upright Flexiscope configuration. Image C and F were taken with the upright/electrophysiology Flexiscope configuration. Image A-C and Image D-F were acquired at the same region of tissue and thus allowed direct comparison of fluorescence performance in each configuration. The high quality performance was consistent for each configuration. Image G-J demonstrates the three channel fluorescent capabilities of the Flexiscope. Image G-J represents the

same region of DRGs dissected from 5 day old rat pups which were cultured as explants for 6 days on flat laminin coated silicone substrates and fixed in PFA. Image G demonstrates NFH immunolabelling to visualise axonal outgrowth. Image H represents immunolabelling for S100β to visualise cytoplasm of the cell bodies of migrating Schwann cells. Image I demonstrates DAPI (nuclei marker) staining. Image J is an overlay of Image G-I. Scale bar for all images: 50μm.

The use of whole mount prepared *P. pileus* tissue served as an appropriate stress test for our system as the complex 3D topography of the tissue requires Z-stacking. Fluorescence imaging in all three configurations was tested with this tissue preparation at the same position to allow direct comparison (Figure 6 A-F). No apparent difference in the quality of images produced by the system was observed between the three configurations.

The triple fluorescent labelling of the DRGs allowed us to test the performance of the manually swappable filter cubes and assess if multi-channel imaging of a sample at the same location is possible. The system was capable of three channel imaging (Figure 6 G-I) and subsequent alignment to produce a composite image (Figure 6 J). This demonstrates three channel fluorescent capabilities of the system.

OIR was tested in the upright/electrophysiology configuration (Figure 4. E-H, Supplementary Video 3). This technique allowed clear visualisation of unstained *P. pileus* tissue and the 3D topography of the tissue was discernible. This approach also allows for the clear visualisation of the electrode tip, critical for electrophysiological applications (Supplementary Video 2).

3.2 Validation of Automated Stage Scanning and Image Acquisition

The requirements for the automated specimen scanning stage included; relatively low cost, reasonably fast speed of motion, repeatability of motion and multi-functionality (ability to also function as a micromanipulator).

3.2.1The Piezoelectric Stage

Repeatability in the Z-axis

At each new FOV the Z-axis will move a specific ‘step size’ a defined number of times. This results in a Z-stack of images in which the 3D qualities of the tissue can be

appreciated as a maximum intensity projection (Forster et al., 2004) (Figure 2 C). The distance travelled by the piezoelectric actuators with each 'step size' is dependent on many factors including; the resistive torque against which the actuator tip is pushing, drive voltage, step rate, active preload, variance in the frictional behaviour of assembly components and actuation direction/condition (Thorlabs, 2017b). The 'step size' values used by the APT software are arbitrary, therefore we needed to determine the distance in μm these values equated to. We also wanted to test the repeatability of each step size as it is reported that the distance may vary up to +/-20% with each step (Thorlabs, 2017a).

Videos were acquired of the stage in motion to determine the distance travelled for 'step sizes' of 1000, 500, 250, 50 and 20 (Figure 2 B). The mean distance (μm) over 15 executions of a step was calculated. The intrinsic lack of reliability upon repeating the same command was clearly observed during our testing as seen in Figure 2 B. This is not a major issue for our applications as maximum intensity projections disregard any Z-dimension information. However, repeatability in the Z-axis would enable 3D reconstructions of the Z-stacks (for example, Fiji's Z-project (Schindelin et al., 2012)) and therefore a different motor should be utilised to achieve this. In addition, the distance travelled when the stage is moving up is greater than the distance travelled when the stage is moving down, despite the same distance command being sent to the actuators.

Z-axis Error Correction

As mentioned in 3.1, imaging the structurally complex 3D topography of *P. pileus* tissue endows many challenges including the fact that the focal plane of the tissue will vary throughout the sample. This factor in combination with the discrepancy in distance travelled when the stage is moving up/down resulted in the need for the implementation of a Z-correction mechanism. A previously described auto-focus algorithm (Geusebroek et al., 2000) was implemented on all the images in every Z-stack. This enabled a correction factor in the Z-axis to be implemented prior to the next Z-stack acquisition. Over time without the use of this Z-correction the Z-stack images would not contain any in focus regions and thus this was an effective solution to this problem.

Large Composite Image Generation

An example of a tissue scan composite is seen in Figure 2 E and demonstrates automated stage scanning capabilities. This demonstrates the nerve net in *P. pileus* as described in 3.1. This composite is a combination of 50 images acquired at 20X with each image comprising a maximum intensity projection from 20 images (generated using stitching algorithm ImageJ: (Preibisch et al., 2009)). This scanning capability not only enables significant time saving (as opposed to performing this manually) but it also enables an appreciation of information flow and overall context of the network which is otherwise lost with sub-sampling small regions of the nerve net.

Repeatability in the X and Y dimensions

The X and Y-actuators where tested and optimised for 20X and 4X objectives to determine the appropriate travel distance to achieve a new 'FOV' with sufficient overlap for subsequent image stitching. The X and Y axes FOV overlap at 20X was established at 25% and 30% respectively (Figure 2 D). This overlap value can be decreased or increased depending on the specific application/tissue by editing the distance command in the code. The lack of repeatability of the piezoelectric actuators was also observed in the X and Y axes, however, the overlap is large enough to overcome this inconsistency using feature matching stitching algorithms rather than a XY coordinate approach (Preibisch et al., 2009).

3.2.2 The Stepper Motor Stage

The stepper motor stage aimed to improve the speed and repeatability of the piezoelectric configuration. The X and Y axes had a FOV overlap at 20X of 10% and this was sufficient to enable subsequent image stitching. This system could translate to a new FOV in the X-dimension at 4X magnification in 15 seconds (as opposed to 290s in the piezoelectric assembly). This assembly costs €1666 as opposed to €4539 for the piezoelectric system. The discrepancy between actual distance travelled and the Gcode distance command was -2% and up to +18.5% (Supplementary Table Figure 2). This was most likely due a mechanical issue (3D printed coupling components not perfectly aligned) rather than a motor or software issue. Vibration during motion was observed and indicates that this configuration wouldn't be suitable

as a micromanipulator. The advantages of this system as compared to the piezoelectric system include cost and speed of imaging.

3.3 Validation of Piezoelectric Actuators as a Micromanipulator in Four Dimensions

As described above, the same approach was taken to determine the distance (μm) travelled when commands of a specific 'step size' were sent to the piezoelectric actuators, now configured as a micromanipulator (Figure 5 A), to ensure the effect of a different load was accounted for. Precise electrode control in four directions was achieved (Figure 5, Supplementary Video 2). Figure 5 outlines validation of the piezoelectric actuators as a micromanipulator for electrophysiological recordings. These actuators are described as being ideal for set and hold applications as they are self-locking and no power is required to hold position (Thorlabs, 2017a). We therefore tested stability of the electrode position over time as this is crucial during intracellular electrophysiology experiments. At a resolution of 1.85μm per pixel, no drift was observed over 16 hours with the power off. The lack of repeatability is not a major issue for micromanipulation applications.

4. Discussion

We have provided a detailed description of the Flexiscope, a modular custom-built microscopy and electrophysiology system which is tailored to the specific needs of our research and successfully achieved substantial cost savings. This system could be replicated or adapted for the specialised needs of any researcher.

4.1 Limitations

A small number of limitations of the system were noted over many months of extensive use. Dust can be easily introduced to the system during assembly and reconfiguration; even with care this seems inevitable, although deconstruction for cleaning should actually be easier than pre-assembled commercial systems. Wear/tear and potential damage due to repeated handling of the various elements is a possibility but any damage to a specific element can be easily replaced at a relatively low cost. In contrast, replacing a specific element of a commercial microscope is expensive and

often must be performed by an engineer. The most significant issue noted with our system is uneven illumination observed in our fluorescent images, however this has been described as a common problem in many commercial systems (Leong et al., 2003). In addition, during motion the piezoelectric actuators were slow and produced a high-pitched sound. We would suggest to any researchers wanting to replicate our piezoelectric automated stage scanning set up to consider purchasing a different motion control actuator. Our script could be incorporated into any XYZ motion control system by simply substituting the motion control command lines with an alternative command. This script could also be adapted for time lapse imaging of multiple regions within a sample or for automated behaviour tracking.

4.2 Replace Mechanical Coupling Components with 3D printed Components

A key motivation behind this design is to reduce costs as far as possible while still maintaining performance. The next step in cost reduction would be to replace some of the prefabricated components with 3D printed components. While obviously critical optical components (lenses, mirrors, filters) of the system cannot be 3D printed easily, we wanted to know if the structural components, such as lens tubes, could be replaced by 3D printed parts to further reduce cost. A length adjustable 1” 3D printed lens tube (3D1, 3D2) was printed in black PLA filament on an Ultimaker Original printer and incorporated into our system replacing the aluminium lens tubes in the camera module. Black PLA was used to reduce the influence of reflections within the light path. In terms of the OIR microscopy, no difference in quality was observed (Supplementary Figure 1 C and F). However, when performing fluorescent microscopy the exposure time needed to be four times higher compared to the original upright configuration in order to visualise the tissue. This resulted in an increase in the signal to noise ratio and a loss of sharpness (Supplementary Figure 1 B and E). This indicates that the quality of the OIR microscopy is not reliant on the commercial 1” lens tubes and this technique could be implemented with 3D printed coupling components. However, this was not the case for fluorescent microscopy and the commercially available coupling components are important for high quality images, although the exact reason for this is not clear. Future studies would involve replacing other commercial mechanical coupling components with 3D printed components to determine if major cost savings could be achieved with comparable image quality.

4.3 Comparison to Other Modular Microscopes

There are few microscopy systems which can be directly compared to our system. In terms of the ability to alter the light path to configure the objective in the upright or inverted configuration, this has been described once previously (Nguyen et al., 2016). Other modular epi-fluorescent (Beltran-Parrazal et al., 2014), confocal (Ye and McCluskey, 2016) and scanning two-photon (Rosenegger et al., 2014) microscopy systems have also been described. However, our system advantage lies specifically in the ability to designate multiple roles to specific components and alter what aspect of the system is fixed or translating in each configuration. This allows us to achieve the capabilities of multiple microscopes at a considerably lower cost.

5. Conclusion

The configurations described here are only three of the many potential configurations of the Flexiscope. Our system could be directly replicated by the reader or this study could be used as inspiration for any research group to establish their own custom Flexiscope. Depending on the needs and financial resources of the user, a stripped back version or an upgraded model could be implemented. For example, if the user only requires one channel of fluorescence, a considerable reduction in cost would be achieved. The modular nature of the system means that as technologies improve, or as additional funding becomes available, new components can be incorporated or replaced over time as the needs of the team evolves. Innovation and flexibility in experimental design are paramount to the advancement of neuroscience.

6. Acknowledgements

This work is financially supported by School of Medicine, University College Dublin. The authors also wish to acknowledge Dominic Courtney for his invaluable assistance in the collection of ctenophores.

Bibliography

ALIX, P., WINTERER, J. & MÜLLER, W. 2003. New illumination technique for IR-video guided patch-clamp recording from neurons in slice cultures on biomembrane. *Journal of Neuroscience Methods,* 128**,** 79-84.

BADEN, T., CHAGAS, A. M., GAGE, G., MARZULLO, T., PRIETO-GODINO, L. L. & EULER, T. 2015. Open Labware: 3-D Printing Your Own Lab Equipment. *PLoS Biology,* 13**,** e1002086.

BELTRAN-PARRAZAL, L., MORGADO-VALLE, C., SERRANO, R. E., MANZO, J. & VERGARA, J. L. 2014. Design and construction of a modular low-cost epifluorescence upright microscope for neuron visualized recording and fluorescence detection. *J Neurosci Methods,* 225**,** 57-64.

CYBULSKI, J. S., CLEMENTS, J. & PRAKASH, M. 2014. Foldscope: Origami-Based Paper Microscope. *PLOS ONE,* 9**,** e98781.

FORSTER, B., VAN DE VILLE, D., BERENT, J., SAGE, D. & UNSER, M. 2004. Complex wavelets for extended depth-of-field: A new method for the fusion of multichannel microscopy images. *Microscopy Research and Technique,* 65**,** 33-42.

GEUSEBROEK, J.-M., CORNELISSEN, F., SMEULDERS, A. W. M. & GEERTS, H. 2000. Robust autofocusing in microscopy. *Cytometry,* 39**,** 1-9.

HERNANDEZ-NICAISE, M. L. 1973. [The nervous system of ctenophores. I. Structure and ultrastructure of the epithelial nerve-nets]. *Z Zellforsch Mikrosk Anat,* 137**,** 223-50.

HERNÁNDEZ VERA, R., SCHWAN, E., FATSIS-KAVALOPOULOS, N. & KREUGER, J. 2016. A Modular and Affordable Time-Lapse Imaging and Incubation System Based on 3D-Printed Parts, a Smartphone, and Off-The-Shelf Electronics. *PLOS ONE,* 11**,** e0167583.

JAGER, M., CHIORI, R., ALIE, A., DAYRAUD, C., QUEINNEC, E. & MANUEL, M. 2011. New insights on ctenophore neural anatomy: immunofluorescence study in Pleurobrachia pileus (Muller, 1776). *J Exp Zool B Mol Dev Evol,* 316b**,** 171-87.

JORGENSON, L. A., NEWSOME, W. T., ANDERSON, D. J., BARGMANN, C. I., BROWN, E. N., DEISSEROTH, K., DONOGHUE, J. P., HUDSON, K. L., LING, G. S. F., MACLEISH, P. R., MARDER, E., NORMANN, R. A., SANES, J. R., SCHNITZER, M. J., SEJNOWSKI, T. J., TANK, D. W., TSIEN, R. Y., UGURBIL, K. & WINGFIELD, J. C. 2015. The BRAIN Initiative: developing technology to catalyse neuroscience discovery. *Philosophical Transactions of the Royal Society B: Biological Sciences,* 370**,** 20140164.

LEONG, F. J. W. M., BRADY, M. & MCGEE, J. O. D. 2003. Correction of uneven illumination (vignetting) in digital microscopy images. *Journal of Clinical Pathology,* 56**,** 619-621.

MAIA CHAGAS, A., PRIETO-GODINO, L. L., ARRENBERG, A. B. & BADEN, T. 2017. The €100 lab: A 3D-printable open-source platform for fluorescence microscopy, optogenetics, and accurate temperature control during behaviour of zebrafish, Drosophila, and Caenorhabditis elegans. *PLOS Biology,* 15**,** e2002702.

NGUYEN, V., RIZZO, J. & SANII, B. 2016. An Assemblable, Multi-Angle Fluorescence and Ellipsometric Microscope. *PLoS ONE,* 11**,** e0166735.

PEIDLE, J., STOKES, C., HART, R., FRANKLIN, M., NEWBURGH, R., PAHK, J., RUECKNER, W. & SAMUEL, A. 2009. Inexpensive microscopy for introductory laboratory courses. *American Journal of Physics,* 77**,** 931-938.

PREIBISCH, S., SAALFELD, S. & TOMANCAK, P. 2009. Globally optimal stitching of tiled 3D microscopic image acquisitions. *Bioinformatics,* 25**,** 1463-1465.

ROSENEGGER, D. G., TRAN, C. H. T., LEDUE, J., ZHOU, N. & GORDON, G. R. 2014. A High Performance, Cost-Effective, Open-Source Microscope for Scanning Two-Photon Microscopy that Is Modular and Readily Adaptable. *PLoS ONE,* 9**,** e110475.

RUEDEN, C. T., SCHINDELIN, J., HINER, M. C., DEZONIA, B. E., WALTER, A. E., ARENA, E. T. & ELICEIRI, K. W. 2017. ImageJ2: ImageJ for the next generation of scientific image data. *BMC Bioinformatics,* 18**,** 529.

SCHINDELIN, J., ARGANDA-CARRERAS, I., FRISE, E., KAYNIG, V., LONGAIR, M., PIETZSCH, T., PREIBISCH, S., RUEDEN, C., SAALFELD, S., SCHMID, B., TINEVEZ, J.-Y., WHITE, D. J., HARTENSTEIN, V., ELICEIRI, K., TOMANCAK, P. & CARDONA, A. 2012. Fiji: an open-source platform for biological-image analysis. *Nature Methods,* 9**,** 676.

SHARKEY, J. P., FOO, D. C. W., KABLA, A., BAUMBERG, J. J. & BOWMAN, R. W. 2016. A one-piece 3D printed flexure translation stage for open-source microscopy. *Review of Scientific Instruments,* 87**,** 025104.

STEWART, C. & GIANNINI, J. 2016. Inexpensive, Open Source Epifluorescence Microscopes. *Journal of Chemical Education,* 93**,** 1310-1315.

THORLABS 2017a. PIA Series Piezo Inertia Actuators: User Guide (HA0360T Rev C Feb 2017). 1 Saint Thomas Place, Ely Cambridgeshire CB7 4EX, UK.

THORLABS 2017b. TIM101 Piezo Inertia Motor Controller: User Guide (HA0195T Rev A Jun 2017). 1 Saint Thomas Place, Ely Cambridgeshire CB7 4EX, UK.

YE, X. & MCCLUSKEY, M. D. 2016. Modular Scanning Confocal Microscope with Digital Image Processing. *PLOS ONE,* 11**,** e0166212.

Supplementary Figure 1. Replacing Opto-mechanical Elements with 3D Printed Components: Fluorescence and OIR Microscopy Comparison.

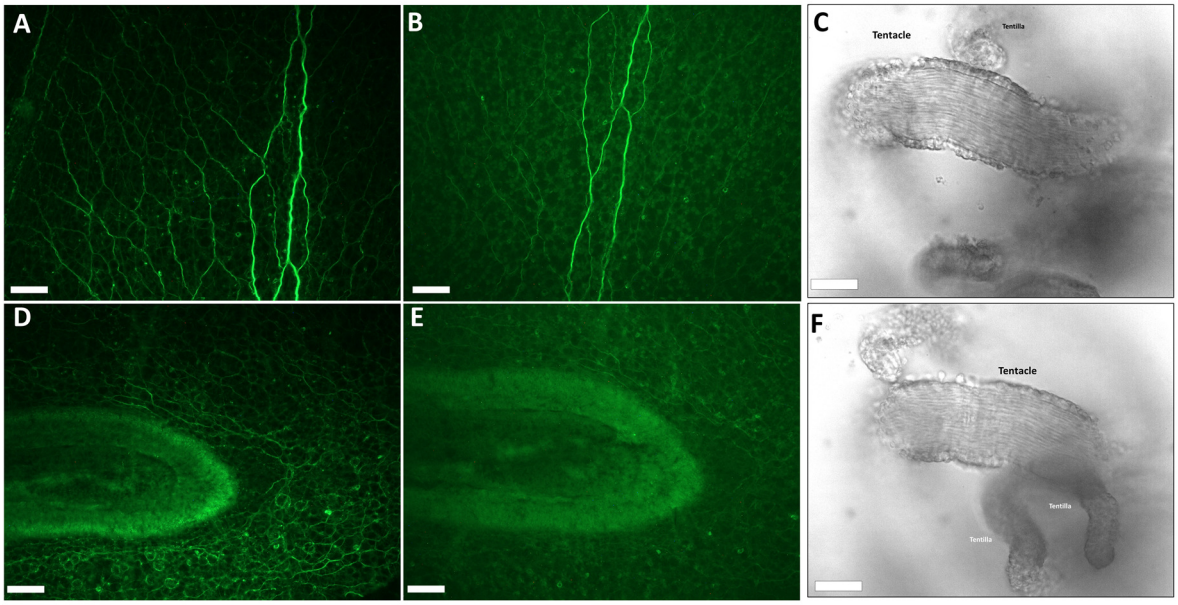

Fixed whole mount *P. pileus* (gelatinous marine invertebrate) were labelled with an antibody against anti-tyrosylated α-tubulin. Image A and D were acquired with the upright Flexiscope configuration with all commercial optomechanical components. Image B and E were acquired with the upright configuration and CO35 and CO37 were replaced with an adjustable 1" 3D printed lens tube. Exposure time was set at 2000ms for Image A/D and 8000ms for Image B/E. Image A/B and Image D/E were taken at the same region of tissue. This comparison was undertaken to determine if further cost savings could be achieved by replacing commercial optomechanical components with 3D printed components. Image C and F demonstrates the ability of the upright configuration with the 3D printed component to perform OIR microscopy on the tentacle of *P. pileus*. Image E and F can be directly compared with Figure 4 E-G. Scale bar: 50μm.

Supplementary Figure 2. Validation of Automated Specimen Stage Stepper Motor Motion Control and Image Acquisition.

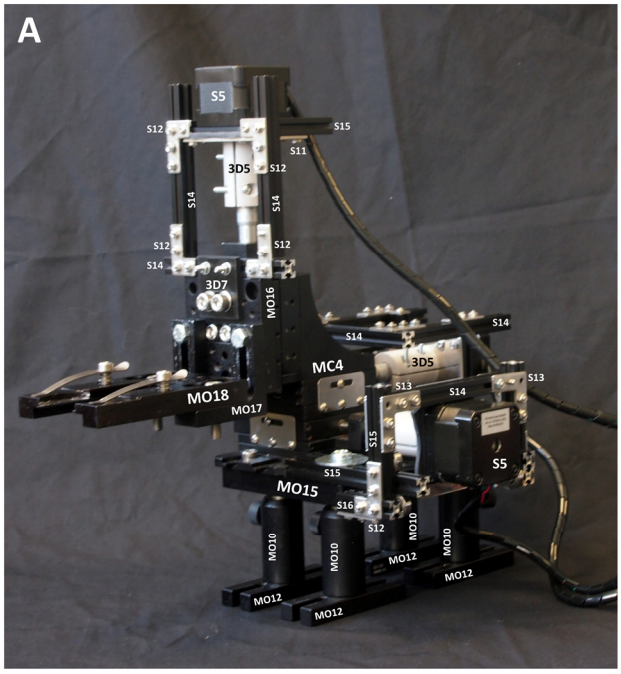

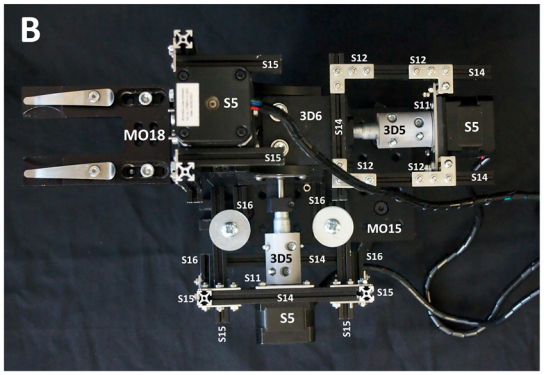

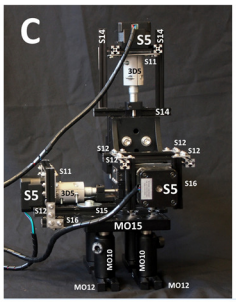

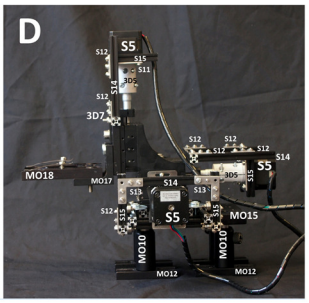

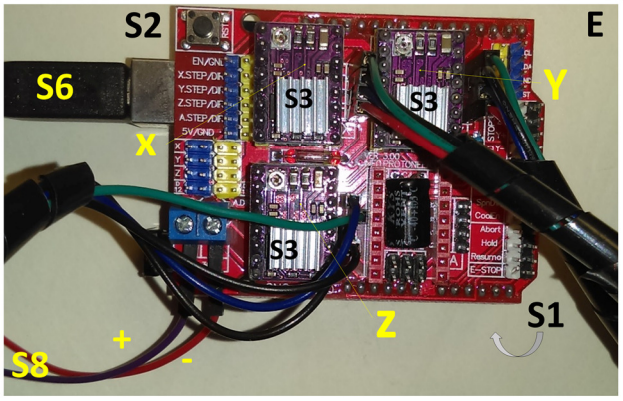

Axis and Direction	Gcode Distance Command (µm)	Mean Distance Travelled (µm)	Distance Discrepancy (µm)	*Error Distance Discrepancy (%)
Z +	20	21.16	1.16	5.8
Z-	20	21.42	1.42	7.1
Z+	6	6.95	0.95	15.8
Z-	6	7.11	1.11	18.5
X+	2200	2155.76	-44.24	-2
X-	2200	2184.61	-15.39	-0.7
X+	430	442.69	12.69	3
X-	430	423.07	-6.93	-1.6
X+	800	761.82	-38.18	-4.8
X-	800	767.56	-32.44	-4.1
Y+	1600	1578.84	-21.16	-1.3
Y-	1600	1581.73	-18.27	-1.1
Y+	600	567.29	-32.71	-5.5
Y-	600	577.16	-22.84	-3.8
Y+	320	327.3	7.3	2.3
Y-	320	316.34	-3.66	-1.1

This is the second iteration of the Automated Specimen Stage Motion Control and Image Acquisition system, this assembly utilises stepper motors as opposed to piezoelectric actuators. Photographs of the stage in which motion was controlled with stepper motors (A-D). E outlines the hardware controlling this system. The table details the Gcode commands sent to specific axes and how much discrepancy observed in distance travelled. Videos were acquired of the stage during motion and the distance was manually calculated in ImageJ (Rueden et al., 2017). This stage is faster and cheaper when compared to the piezoelectric assembly. *Error distance discrepancy = distance discrepancy/Gcode distance command×100=%.

Supplementary Video 1. Timelapse Video Demonstrating How to Transition from the Inverted to the Upright Configuration of the Flexiscope in Under 24 Minutes. Note the timer at the bottom left of the screen.

Supplementary Video 2. Piezoelectric Four Dimension Micromanipulator Validation: Demonstrating the Performance of the Approach-Axis on a Tissue Sample. Stage was configured as seen in Figure 4. Fixed *P. pileus* (gelatinous marine invertebrate) was visualised using OIR microscopy. The following parameters were set through the APT software for the piezoelectric actuator; voltage (V): 110, drive rate (steps/sec): 500, drive accn (steps/sec/sec): 100000 and jog rate (steps/sec):100. A step size of 100 was executed five times in towards the tissue (Move + 1.8µm) and out away from the tissue (Move – 2.04µm). This video demonstrates capability of the piezoelectric actuators to accurately manipulate a glass electrode for electrophysiology experiments. Scale bar: 50µm.

Supplementary Video 3. Demonstrating OIR Microscopy Capabilities of the System to Visualise Unstained Tissue. OIR microscopy is performed by simply positioning Infrared LEDs obliquely above or below the tissue. This technique allowed us to visualise the tentacular sheath within a live, intact *P. pileus* (gelatinous marine invertebrate). The movement of the tissue visible in the video is a result of beating of the ciliary comb plates. 3D tissue structure and muscular contractions in a live unstained animal can be visualised. Scale bar: 500µm.

Supplementary File 1. Matlab Code and Assembly/Operation Guidelines for the Automated Piezoelectric Motor Stage.

Supplementary File 2. Matlab Code and Assembly/Operation Guidelines for the Automated Stepper Motor Stage.

Supplementary File 3. 3D Printed Components (stl files).